

Na₂ Vibrating in the Double-Well Potential of State 2 ¹Σ_u⁺ (*JM* = 00): A Pulsating “Quantum Bubble” with Antagonistic Electronic Flux

Published as part of *The Journal of Physical Chemistry* virtual special issue “Manuel Yáñez and Otilia Mó Festschrift”.

D. J. Diestler,^{†,‡,§,||} D. Jia,[§] J. Manz,^{*,†,§,||} and Y. Yang^{§,||}

[†]Institut für Chemie und Biochemie, Freie Universität Berlin, 14195 Berlin, Germany

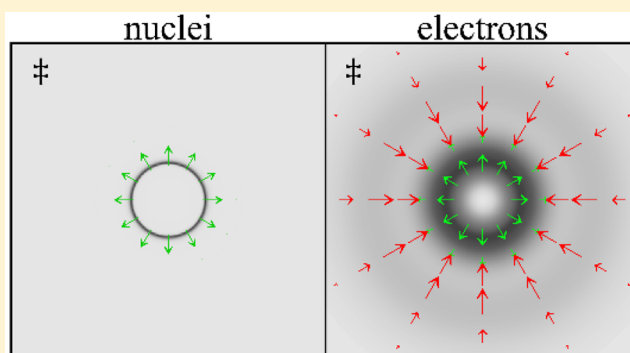
[‡]University of Nebraska—Lincoln, Lincoln, Nebraska 68583, United States

[§]State Key Laboratory of Quantum Optics and Quantum Optics Devices, Institute of Laser Spectroscopy, Shanxi University, Taiyuan 030006, China

^{||}Collaborative Innovation Center of Extreme Optics, Shanxi University, Taiyuan 030006, China

S Supporting Information

ABSTRACT: The theory of concerted electronic and nuclear flux densities associated with the vibration and dissociation of a multielectron nonrotating homonuclear diatomic molecule (or ion) in an electronic state ^{2S+1}Σ_{g,u}⁺ (*JM* = 00) is presented. The electronic population density, nuclear probability density, and nuclear flux density are isotropic. A theorem of Barth, presented in this issue, shows that the electronic flux density (EFD) is also isotropic. Hence, the evolving system appears as a pulsating, or exploding, “quantum bubble”. Application of the theory to Na₂ vibrating in the double-minimum potential of the 2 ¹Σ_u⁺ (*JM* = 00) excited state reveals that the EFD consists of two antagonistic components. One arises from electrons that flow essentially coherently with the nuclei. The other, which is oppositely directed (i.e., antagonistic) and more intense, is due to the transition in electronic structure from “Rydberg” to “ionic” type as the nuclei traverse the potential barrier between inner and outer potential wells. This “transition” component of the EFD rises and falls sharply as the nuclei cross the barrier.



1. INTRODUCTION

The most complete characterization of an *electronically adiabatic* molecular process (the vibration of a diatomic molecule, for an elementary instance) should tell us not only where the electrons and nuclei are at any instant (i.e., probability (population) densities) but also how they get there (i.e., flux densities). However, except in special cases, the *electronic* flux density, in particular, is beyond the reach of standard computational techniques based on the Born–Oppenheimer approximation (BOA). Indeed, it is a new special case that this work deals with: vibrating or dissociating, but nonrotating (*JM* = 00), *multielectron* homonuclear diatomic molecules, such as Na₂.

A previous article¹ reports the results of a study of concerted electron–nuclear dynamics in the *one-electron* system H₂⁺ prepared in the special state ²Σ_g⁺ (*JM* = 00), for which the corresponding wave function is expressed in the BOA as

$$\Psi(\mathbf{r}, \mathbf{R}, t) = \Psi_e(\mathbf{r}; \mathbf{R}) \Psi_n(\mathbf{R}, t) \quad (1.1)$$

In eq 1.1 **r** stands for the position of the electron relative to the nuclear center of mass (NCM) and **R** for the distance vector from one proton to the other, $\Psi_e(\mathbf{r}; \mathbf{R})$ is the ground-state

electronic energy eigenfunction, and the nuclear wave packet is assumed to be spherically symmetric

$$\begin{aligned} \Psi_n(\mathbf{R}, t) &= Y_{00}(\theta, \phi) R^{-1} \chi(R, t) \\ &= (4\pi)^{-1/2} R^{-1} \chi(R, t) \end{aligned} \quad (1.2)$$

The subscript 00 on the spherical harmonic function corresponds to *JM* = 00. The consequence is that the nuclear probability and flux densities are isotropic (i.e., spherically symmetric) about the NCM. The electronic probability and flux densities are likewise isotropic. Hence, when the total energy is below the threshold for dissociation, the evolving system appears as a pulsating “quantum bubble”: all probability densities and flux densities remain spherically distributed about the NCM. At energies above threshold the “quantum bubble” explodes.^{2,3}

In section 2 we outline the extension of the theory for the *one-electron* nonrotating homonuclear diatomic to the general case of

Received: November 29, 2017

Revised: January 24, 2018

Published: January 24, 2018



the *multielectron* nonrotating homonuclear diatomic in the state $2^{S+1}\Sigma_{\text{gu}}^+$ ($JM = 00$). We show that the rotational quantum numbers $JM = 00$ imply isotropy of the nuclear probability and flux densities, as well as that of the electronic *population* density and we infer from this agreement with the one-electron case that the electronic *flux* density is also isotropic. (A rigorous proof of this property is presented in this volume by Ingo Barth.⁴) The isotropy of all densities and fluxes means that the nonrotating multielectron homonuclear diatomic molecule evolves as a pulsating “quantum bubble”, irrespective of the number of electrons.

Our choice of the specific system, Na_2 vibrating in the double-well potential of the $2^1\Sigma_{\text{u}}^+$ state, is motivated by several prior investigations of its electronic structure,^{5–7} and by the search for the properties and dynamical consequences of the double minimum,^{8–18} both theoretically^{10–18} and experimentally.^{8,9,15–17} Valance and Nguyen Tuan, who first discovered the double-well, noted that the inner and outer wells have different electronic configurations.⁵ The quantum chemical analysis of Jeung attributes the phenomenon to the avoided crossing of two neighboring electronic states with the same symmetry but different electronic structures.⁶ According to Vergès et al.,⁷ the resulting inner and outer potential wells of the $2^1\Sigma_{\text{u}}^+$ state have dominant (though not perfect⁸) Rydberg and ionic character, respectively. Because these labels have been adopted in the subsequent literature,^{9–17} we use them in the present context. The main purpose of Vergès et al.^{7,8} was to determine the shape of the double-minimum potential accurately by inversion of Fourier transform spectra.

Subsequently, efforts to tease out the implications of the transformation of the electronic structure for dynamical properties have been made. For example, Arasaki et al. predicted that the electronic-structure change should induce significant changes in dipole transitions from the $2^1\Sigma_{\text{u}}^+$ state to the ground state and to excited ionic states, which in turn should be reflected in the energy-, angle-, and (femtosecond) time-resolved photoelectron spectra.^{10–14} Their theoretical results stimulated experimental two-color femtosecond pump–probe photoelectron spectroscopy designed to monitor the nuclear wave packet dynamics in the double-minimum potential of the $2^1\Sigma_{\text{u}}^+$ state of Na_2 .¹⁵ Wollenhaupt et al.¹⁵ observe bound-to-ionic ionization probability four times greater at the outer (“ionic”) classical turning point than at the inner (“Rydberg”) turning point (see also refs 9, 16, and 17).

In a recent article several of us announced the discovery of a novel consequence for the electron dynamics (namely the occurrence of *antagonistic*, or oppositely directed, electron fluxes in contiguous regions) due to transformation of the electronic structure in the $2^1\Sigma_{\text{u}}^+$ ($JM = 00$) state of Na_2 that occurs as the nuclei cross the potential barrier.¹⁸ Section 3 provides a detailed analysis of the phenomenon based on the theoretical development of section 2. The essential idea is that the rapid change of electronic structure at the barrier between the inner and outer potential wells should be accompanied by significant rearrangement of the electronic population density, and this rearrangement, in turn, should be reflected in the electronic flux. In other words, one should observe a strong isotropic electronic flux density as the nuclei traverse the potential barrier. We stress that this flux due to the electronic structural change is complementary to the “normal” flux of the electrons that travel more or less coherently with the nuclei.³ Analogous strong electronic fluxes due to *non*-adiabatic transitions, or “surface hopping” between

different electronic states, have already been reported by Takatsuka and co-workers.^{19–22} In contrast, the present work documents strong electronic flux density during *adiabatic* passage over the barrier between the “Rydberg” and “ionic” structures. The results for the $2^1\Sigma_{\text{u}}^+$ ($JM = 00$) state of Na_2 are presented and discussed in section 3. Our conclusions are summarized in section 4.

2. THEORY

We consider an isolated generic homonuclear diatomic molecule or molecular ion that can be adequately described by nonrelativistic quantum mechanics. In terms of center-of-mass coordinates we can write the *internal* Hamiltonian (i.e., the Hamiltonian exclusive of the *total* center of mass) as

$$H = H_{\text{e}} + T_{\text{n}} = T_{\text{e}} + V(\mathbf{r}^{N_{\text{e}}}, \mathbf{R}) + T_{\text{n}} \quad (2.1)$$

where the electronic Hamiltonian H_{e} is defined implicitly, $V(\mathbf{r}^{N_{\text{e}}}, \mathbf{R})$ is the Coulombic potential energy of interaction of all particles,

$$T_{\text{e}} = -\frac{\hbar^2}{2m_{\text{e}}} \sum_{i=1}^{N_{\text{e}}} \nabla_{\mathbf{r}_i}^2 \quad (2.2\text{a})$$

is the electronic kinetic energy operator and

$$T_{\text{n}} = -\frac{\hbar^2}{2\mu_{\text{n}}} \nabla_{\mathbf{R}}^2 \quad (2.2\text{b})$$

is the nuclear kinetic energy operator. The reduced mass of the nuclei is $\mu_{\text{n}} = M/2$, where M is the nuclear mass. In eqs 2.1 and 2.2 $\mathbf{r}^{N_{\text{e}}}$ stands for the configuration of the N_{e} electrons with respect to the nuclear center of mass (NCM) and \mathbf{R} for the distance vector between the nuclei. The derivation of eqs 2.2 also invokes the following approximations³ (see also Appendix A of the Supporting Information): the center of mass of the whole system is replaced by the NCM; the mass-polarization contribution to H_{e} is ignored; the reduced mass of the electron is replaced by its mass, m_{e} ; spin is ignored, except for the implicit requirement that the eigenfunctions of H_{e} obey the Pauli exclusion principle.

We assume that the molecule is in a state fully characterized by the BOA wave function

$$\Psi(\mathbf{r}^{N_{\text{e}}}, \mathbf{R}, t) = \Psi_{\text{e}}(\mathbf{r}^{N_{\text{e}}}, \mathbf{R}) \Psi_{\text{n}}(\mathbf{R}, t) \quad (2.3)$$

which is analogous to the one-electron wave function in eq 1.1. The BOA is justified by noting that for the particular system of interest, namely, Na_2 vibrating in the double-well potential of the $2^1\Sigma_{\text{u}}^+$ state, the kinetic energy in the vicinity of the potential barrier, where the electronic structure undergoes a strong transformation, is about an order of magnitude smaller than the energy gaps between the neighboring potential curves. The consequence is that the nonadiabatic coupling to neighboring electronic states is negligible, in accord with refs 10–17. The electronic wave function Ψ_{e} obeys the electronic energy eigenvalue equation

$$H_{\text{e}} \Psi_{\text{e}}(\mathbf{r}^{N_{\text{e}}}, \mathbf{R}) = V(R) \Psi_{\text{e}}(\mathbf{r}^{N_{\text{e}}}, \mathbf{R}) \quad (2.4\text{a})$$

where the eigenvalue $V(R)$ is a parametric function of the internuclear distance $R = |\mathbf{R}|$ that serves as potential energy for the nuclear motion. The nuclear wave packet obeys the nuclear Schrödinger equation (SE)

$$i\hbar \frac{\partial \Psi_n(\mathbf{R}, t)}{\partial t} = [T_n + V(R)] \Psi_n(\mathbf{R}, t) \quad (2.4b)$$

Finally, exploiting the zero angular momentum of the nuclear state, we can express the assumed normalized packet conveniently by

$$\Psi_n(\mathbf{R}, t) = Y_{00}(\Theta, \Phi) R^{-1} \chi(R, t) = (4\pi)^{-1/2} R^{-1} \chi(R, t) \quad (2.5)$$

which is the analogue of eq 1.2. The auxiliary packet satisfies the radial SE

$$i\hbar \frac{\partial \chi(R, t)}{\partial t} = \left[-\frac{\hbar^2}{2\mu_n} \frac{\partial^2}{\partial R^2} + V(R) \right] \chi(R, t) \quad (2.6)$$

The electronic *population density* (EPD) is given by

$$\begin{aligned} d_e(\mathbf{r}, t) &= \langle \Psi(t) | \sum_{i=1}^{N_e} \delta(\mathbf{r} - \mathbf{r}_i) | \Psi(t) \rangle \\ &= \int d\mathbf{R} \int d\mathbf{r}^{N_e} \Psi_e(\mathbf{r}^{N_e}; \mathbf{R}) \Psi_n^*(\mathbf{R}, t) \\ &\quad \times \sum_{i=1}^{N_e} \delta(\mathbf{r} - \mathbf{r}_i) \Psi_e(\mathbf{r}^{N_e}; \mathbf{R}) \Psi_n(\mathbf{R}, t) \\ &= \int d\mathbf{R} |\Psi_n(\mathbf{R}, t)|^2 \sum_{i=1}^{N_e} \prod_{j \neq i}^{N_e} \int d\mathbf{r}_j [\Psi_e^2(\mathbf{r}^{N_e}; \mathbf{R})]_{\mathbf{r}_i = \mathbf{r}} \end{aligned} \quad (2.7)$$

where $\int d\mathbf{r}^{N_e} \equiv \prod_{i=1}^{N_e} \int d\mathbf{r}_i = \int d\mathbf{r}_1 \int d\mathbf{r}_2 \dots \int d\mathbf{r}_{N_e}$. (Note that $\int d\mathbf{r} d_e(\mathbf{r}, t) = N_e$, i.e., $d_e(\mathbf{r}, t)$ is normalized to the number of electrons (population).) Transforming the nuclear variables of integration from Cartesian coordinates to spherical coordinates and invoking the indistinguishability of the electrons, we can rewrite eq 2.7 as

$$\begin{aligned} d_e(\mathbf{r}, t) &= (4\pi)^{-1} \int_0^\infty dR |\chi(R, t)|^2 \int_0^{2\pi} d\Phi \\ &\quad \times \int_{-1}^1 d(\cos \Theta) N_e d_{1e,n}(\mathbf{r}; \mathbf{R}) \end{aligned} \quad (2.8)$$

We define the “one-electron” probability density appearing in eq 2.8 by

$$d_{1e,n}(\mathbf{r}; \mathbf{R}) \equiv \prod_{j \neq i}^{N_e} \int d\mathbf{r}_j [\Psi_e^2(\mathbf{r}^{N_e}; \mathbf{R})]_{\mathbf{r}_i = \mathbf{r}} \quad (2.9)$$

which is the *probability* of finding *any* electron in the volume element $d\mathbf{r}$ about the point of observation \mathbf{r} for a *fixed* separation \mathbf{R} between the nuclei. Thus, $N_e d_{1e,n}(\mathbf{r}; \mathbf{R})$ is the *population density* of electrons at \mathbf{r} with \mathbf{R} *fixed* (the semicolon denotes that $d_{1e,n}(\mathbf{r}; \mathbf{R})$ depends parametrically on \mathbf{R}).

If the one-electron probability density possesses cylindrical symmetry, as is the case for the electronic states of interest here, then $d_{1e,n}(\mathbf{r}; \mathbf{R})$ depends only on r , R , and the cosine of the angle γ between \mathbf{r} and \mathbf{R} . But γ is related to the polar angles of \mathbf{r} and \mathbf{R} by the formula

$$\cos \gamma = \cos \Theta \cos \theta + \sin \Theta \sin \theta \cos(\Phi - \phi) \quad (2.10)$$

We now observe that because the integration indicated in the basic formula for $d_e(\mathbf{r}, t)$ (eq 2.7) runs over all possible values of \mathbf{R} , the polar axis of the spherical coordinate frame need not be specified. In other words, the choice of the polar axis is arbitrary.

For convenience, we choose it to lie along the direction of \mathbf{r} (i.e., we take \mathbf{r} to lie along the polar axis parallel with \mathbf{e}_z , the Cartesian unit vector). It follows from eq 2.10 that $\theta = 0$ and therefore that $\cos \gamma = \cos \Theta$. Hence, $d_{1e,n}(\mathbf{r}; \mathbf{R})$ can be expressed as $\delta_{1e,n}(r; R, \cos \Theta)$. (Note that to this juncture the symbol d is used for “density” expressed generally in terms of the vectors \mathbf{r} and \mathbf{R} ; henceforth, the symbol δ is reserved for density expressed in spherical coordinates.) Then eq 2.8 can be rewritten

$$\delta_e(r, t) = (4\pi)^{-1} \int_0^\infty dR |\chi(R, t)|^2 \delta_{e,n}(r; R) \quad (2.11)$$

where, for the sake of convenience, we define the quantity (static electronic population density at *fixed* R)

$$\begin{aligned} \delta_{e,n}(r; R) &\equiv N_e \int_0^{2\pi} d\Phi \int_{-1}^1 d(\cos \Theta) \delta_{1e,n}(r; R, \cos \Theta) \\ &= 2\pi N_e \int_{-1}^1 d(\cos \Theta) \delta_{1e,n}(r; R, \cos \Theta) \end{aligned} \quad (2.12)$$

Equation 2.11 implies that the EPD is isotropic, which is a consequence of the isotropy of the nuclear wave packet (eq 2.5). An alternative, more detailed, demonstration that the EPD is spherically symmetric is given in Appendix A of the [Supporting Information](#).

We note that $\delta_{e,n}(r; R)$ can be regarded as the result of the integration over all solid angles of one vector of *fixed* length *with respect to* another vector of *fixed* length. From the original viewpoint described above, \mathbf{r} is taken to be parallel with \mathbf{e}_z and the integration is taken to run over all solid angles of \mathbf{R} with respect to \mathbf{r} . However, we can as well take \mathbf{R} to be parallel with \mathbf{e}_z and the integration to range over all solid angles of \mathbf{r} with respect to \mathbf{R} . Then eq 2.12 can be recast as

$$\delta_{e,n}(r; R) = 2\pi N_e \int_{-1}^1 d(\cos \theta) \delta_{1e,n}(r, \cos \theta; R) \quad (2.13)$$

Because only the *magnitudes* of \mathbf{r} and \mathbf{R} appear in the integrand, along with the cosine of the angle between \mathbf{r} and \mathbf{R} , we can adopt either perspective in principle. However, from a physical standpoint eq 2.13 provides an illuminating interpretation of the EPD at *fixed* R , as well as a formula that can be readily implemented within the framework of standard quantum chemistry.

The nuclear probability density (NPD) (i.e., the probability per unit volume of observing the internuclear distance in volume element $d\mathbf{R}$ about \mathbf{R}') is given by

$$\begin{aligned} d_n(\mathbf{R}', t) &= \langle \Psi(t) | \delta(\mathbf{R}' - \mathbf{R}) | \Psi(t) \rangle \\ &= \int d\mathbf{R} \int d\mathbf{r}^{N_e} \Psi_e(\mathbf{r}^{N_e}; \mathbf{R}) \Psi_n^*(\mathbf{R}, t) \delta(\mathbf{R}' - \mathbf{R}) \\ &\quad \times \Psi_e(\mathbf{r}^{N_e}; \mathbf{R}) \Psi_n(\mathbf{R}, t) \\ &= |\Psi_n(\mathbf{R}', t)|^2 \\ &= (4\pi R'^2)^{-1} |\chi(R', t)|^2 \end{aligned} \quad (2.14)$$

where the last line follows from eq 2.5 and the (assumed) normalization of the electronic energy eigenfunction: $\int d\mathbf{r}^{N_e} \Psi_e^2(\mathbf{r}^{N_e}; \mathbf{R}) = 1$. As shown in ref 3 (eq 93) (see also ref 1), the probability density of observing nucleus α (= a , b) at distance \mathbf{R}_α from the NCM is related to $d_n(\mathbf{R}, t)$ by

$$d_{n,\alpha}(\mathbf{R}_\alpha, t) = 8d_n(2\mathbf{R}_\alpha, t) = 2 \frac{1}{4\pi R_\alpha^2} |\chi(2R_\alpha, t)|^2 \quad (2.15)$$

As expected, in either frame (observer on either a or b or on the NCM) the NPD is spherically symmetric (i.e., we may set $d_n(\mathbf{R}, t) = \delta_n(R, t)$ and $\dot{d}_{n,\alpha}(\mathbf{R}, t) = \dot{\delta}_{n,\alpha}(R, t)$).

Elsewhere in this issue Barth proves the following theorem: If the molecular wave function satisfies the SE $i\hbar \partial\Psi(t)/\partial t = H\Psi(t)$ and the *total* angular momentum and its *z*-component vanish (i.e., $J = 0$ and $M = 0$), then the electronic and nuclear flux densities are spherically symmetric.⁴ Though the BOA wave function does not obey the SE, it does satisfy the constraints of the theorem *approximately*. Therefore, we assume that the EFD for our state of interest is spherically symmetric. In that case, we immediately have the expression for the radial (i.e., the only nonzero) component

$$j_{e,r}(r, t) = -r^{-2} \int_0^r dr' r'^2 \frac{\partial \delta_e(r', t)}{\partial t} \quad (2.16)$$

which follows from the reduced radial continuity equation (see eq 39 of ref 3).

The nuclear flux density (NFD), i.e., the flux density of one nucleus relative to the other, is given by

$$\begin{aligned} \mathbf{j}_n(\mathbf{R}', t) &= \text{Re}\{\langle \Psi(t) | \delta(\mathbf{R}' - \mathbf{R}) \dot{\mathbf{R}} | \Psi(t) \rangle\} \\ &= \frac{\hbar}{\mu_n} \text{Im}\left\{ \int d\mathbf{R} \int d\mathbf{r}^N \Psi_e(\mathbf{r}^N; \mathbf{R}) \Psi_n^*(\mathbf{R}, t) \right. \\ &\quad \times \delta(\mathbf{R}' - \mathbf{R}) \nabla_{\mathbf{R}} \Psi_e(\mathbf{r}^N; \mathbf{R}) \Psi_n(\mathbf{R}, t) \} \\ &= \frac{\hbar}{\mu_n} \text{Im}\{\Psi_n^*(\mathbf{R}, t) \nabla_{\mathbf{R}} \Psi_n(\mathbf{R}, t)\}_{\mathbf{R}=\mathbf{R}'} \\ &= \hbar/4\pi\mu_n R'^2 \text{Im}[\chi^*(R, t) \partial\chi(R, t)/\partial R]_{R=R'} \mathbf{e}_R \end{aligned} \quad (2.17)$$

where the third line follows from the normalization of $\Psi_e(\mathbf{r}^N; \mathbf{R})$ and from eq 2.5. It can be shown (see eqs 92 and 93 of ref 3) that the flux density of nucleus α with respect to the NCM is

$$\mathbf{j}_{n,\alpha}(\mathbf{R}, t) = 4\mathbf{j}_n(2\mathbf{R}, t) \quad (2.18)$$

As indicated by eqs 2.17 and 2.18, the NFDs in either of the “atomic” (a or b) frames or the NCM frame are spherically symmetric (i.e., $\mathbf{j}_n(\mathbf{R}, t) = j_n(R, t)\mathbf{e}_R$ and $\mathbf{j}_{n,\alpha}(\mathbf{R}, t) = j_{n,\alpha}(R, t)\mathbf{e}_R$).

3. ANTAGONISTIC ELECTRONIC FLUX IN THE $2^1\Sigma_u^+$ ($JM = 00$) EXCITED STATE OF Na_2

The application of the theory to Na_2 begins with the computation of the double minimum potential of the $2^1\Sigma_u^+$ excited state. For this purpose we employ Gaussian 09²³ to solve eq 2.4a for the potential curve $V(R)$ and the electronic eigenfunction $\Psi_e(\mathbf{r}^N; \mathbf{R})$ using the symmetry adapted cluster-configuration interaction (SAC-CI) method²⁴ with Dunning’s correlation consistent-polarized valence triple- ζ basis set augmented with the diffuse functions (aug-cc-pVTZ) basis set.²⁵ The ab initio double-well potential is shown as a continuous line in Figure 1a. The minima of the rather narrow and shallow inner potential well and of the deeper and wider outer well are located at $R_i = 3.8$ Å and $R_o = 6.9$ Å, respectively, and separated by the barrier, whose maximum is at $R_{\ddagger} = 4.9$ Å. The dots in Figure 1a represent the experimental double-well potential determined by Cooper et al. by a refined RKR analysis of high-resolution Fourier transform spectra.⁸ The agreement of the theoretical curve with the experimental data is quite satisfactory. Indeed, we chose the SAC-CI/aug-cc-pVTZ method, after a systematic investigation of a number of other ab initio methods, because it yields the best agreement with

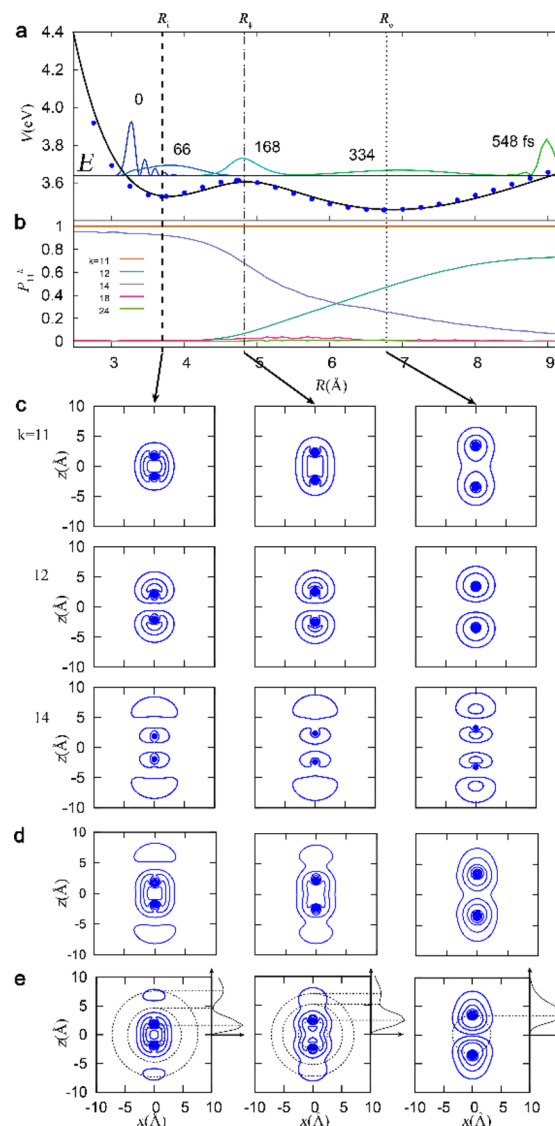


Figure 1. Nuclear and electronic properties of Na_2 in the electronic excited state $2^1\Sigma_u^+$. (a) Double minimum potential curve (solid black line, SAC-CI/aug-cc-pVTZ calculation; dots, experimental data from ref 8). Internuclear distances R_i , R_{\ddagger} , and R_o at the minimum of the inner well, at the top of the barrier, and at the minimum of the outer well are marked by vertical dashed, dash-dotted, and dotted lines, respectively. The horizontal line indicates energy. Also shown are snapshots of nuclear probability density $\delta_n(R, t)$ (weighted by $4\pi R^2$) at times $t = 0$, $t_i = 66$ fs, $t_{\ddagger} = 168$ fs, $t_o = 334$ fs, and $t_{\text{qto}} = 548$ fs, when mean values of R are R_{qto} , R_i , R_{\ddagger} , R_o , and R_{qto} , respectively. (b)–(d) Results of approximate CASSCF-CI(2,36)/aug-cc-pVTZ calculation. (b) Probabilities of the HOMO-to- k excitations, $P_{11}^k(R)$, for the dominant terms in the CI expansion (eq 3.10). (c) Equidistant contour plots of the electronic probability density for HOMO (top), LUMO ($k = 12$, middle), and the excited “Rydberg”-type MO ($k = 14$, bottom) in the x - z plane at internuclear distances R_i (left), R_{\ddagger} (middle), and R_o (right). (d) Equidistant contour plots of the population density $[2d_{1\text{en}}(x, z; R)]$ of valence electrons in the x - z plane, approximated by the sum of MO densities shown (panel c) weighted by occupation probabilities $P_{11}^k(R)$ (panel b). (e) Equidistant contour plots of the SAC-CI/aug-cc-pVTZ population density of valence electrons $[2d_{1\text{en}}(x, z; R)]$ in the x - z plane; plots of $\delta_{\text{en}}(r; R)$ (eq 2.9) versus r oriented at the right-hand boundaries (abscissa is parallel with the z -axis). Values of r at maxima and minimum are indicated by dotted lines, which also indicate intersections of the x - z plane with spherical surfaces on which $\delta_{\text{en}}(r; R)$ is evaluated at these values of r (eq 2.13).

experiment.⁸ This agreement supports the reliability of the electronic properties that we derive on the basis of the SAC-CI/aug-cc-pVTZ method.

Next we focus on the time evolution of the nuclear wavepacket. The two observables of principal interest are the NPD and NFD. Though the time development of the NFD is presented here for the first time, that of the NPD has already been reported.^{9–18} We include the NPD here for several reasons. First, the results for the concerted NPD and EPD, as well as for the NFD and EFD, are based on the potential $V(R)$ and the electronic eigenfunction $\Psi_e(\mathbf{r}^N; \mathbf{R})$, which are obtained by means of one and the same solution of eq 2.4a. Also $V(R)$ agrees well with experiment.⁸ In contrast, previous quantum simulations^{9–17} employ the experimental potential, possibly shifted to yield the known excitation energy and ionization potential. Second, the NPD is an indispensable input to the subsequent calculation of the EPD and EFD (eqs 2.11 and 2.16, respectively). Third, the NPD serves as a reference for discrimination of two branches of the EPD that give rise to two different contributions to the electronic flux (i.e., the “normal” flux that travels with the nuclei and the antagonistic “transition” flux due to the change of electronic structure when the nuclei cross the barrier).

For the quantum simulation of the time evolution of the NPD, we follow the experimental scenario of ref 9, which employs a linearly polarized Gaussian laser pulse with electric field $\varepsilon(t) = E_0 s(t) \cos(\omega_c(t - t_c))$, where $s(t) = \exp[-(t - t_c)^2/2\tau^2]$ is the Gaussian envelope, τ is the pulse duration, and ω_c is the carrier frequency. The constant t_c is arbitrary. The amplitude E_0 is also arbitrary, except that it should be in the weak field limit (i.e., the excitation probability should not exceed a few percent). This restriction avoids interference from such subsequent processes as multiphoton excitation of higher electronic states and ionization. The carrier frequency is related to the experimental wavelength $\lambda = 341.5$ nm by $\omega_c = 2\pi c/\lambda$, where c is the speed of light. The experimental full width at half-maximum (FWHM) of the corresponding intensity $I(t) = \varepsilon_0 c \varepsilon(t)^2$, where ε_0 is the permittivity of the vacuum, is $\text{FWHM} = 2\sqrt{\ln 2} \tau = 60$ fs. Note that the experimental laser parameters of ref 9 differ from those employed in refs 16 and 17 (see Figure 4.9 of ref 16, where $\lambda = 340$ nm and $\text{FWHM} = 35$ fs, values also used in ref 18). The present longer wavelength and duration imply a slightly smaller excitation energy and a significantly narrower spectral width $\Delta\omega = 2\sqrt{\ln 2}/\text{FWHM}$ than that in refs 16–18. As a consequence, the present nuclear wave packet is broader, and the present period of the strongly anharmonic nuclear motion with energy just above the potential barrier is slightly longer, compared with those of refs 16–18.

At the end of the laser excitation the time is set to zero, and the initial ($t = 0$) nuclear wave function is determined as in ref 16 (for details, see Appendix C of the Supporting Information):

$$\chi(R, 0) = \sum_v c_v \chi_{ev}(R) \quad (3.1)$$

where the subscript ev denotes the v th vibrational eigenstate of the electronic excited state $e = 2^1\Sigma_u^+$, and the expansion coefficients are given by

$$c_v = N \langle \chi_{ev} | \chi_{00} \rangle \exp[-(\omega_v - \omega_c)^2 \text{FWHM}^2 / 8 \ln(2)] \quad (3.2)$$

In eq 3.2 $\omega_v = (E_{ev} - E_{00})/\hbar$, where E_{00} is the vibronic ground-state energy. The Franck–Condon factors $\langle \chi_{ev} | \chi_{00} \rangle (= \int dR \chi_{ev}(R) \chi_{00}(R))$ for the transition from the vibronic

ground state (00) to the excited state (ev) is multiplied by a Gaussian filter that selects the vibrational states χ_{ev} with energy E_{ev} close to the carrier photon energy $\hbar\omega_c$. The coefficients are normalized by the factor N such that $\sum_v c_v^2 = 1$. The vibrational eigenfunctions χ_{ev} and energies E_{ev} are solutions of the eigenvalue equation

$$[T_n + V(R)]\chi_{ev}(R) = E_{ev}\chi_{ev}(R) \quad (3.3)$$

which is solved by means of the Fourier grid Hamiltonian method²⁶ on a uniform grid with 1001 points in the domain $2.4 \text{ \AA} \leq R \leq 12.4 \text{ \AA}$.

The solution of the nuclear SE (eq 2.6) is expressed as

$$\chi(R, t) = \sum_v c_v \exp(-iE_{ev}t/\hbar) \chi_{ev}(R) \quad (3.4)$$

The mean energy of the relative nuclear motion,

$$E = \sum_v c_v^2 E_{ev} \quad (3.5)$$

is indicated by the horizontal line in Figure 1a. The energy gap between E and the ground-state energy E_{00} is close to the carrier photon energy, i.e.,

$$(E - E_{00}) \simeq \hbar\omega_c \quad (3.6)$$

The intersections $E = V(R_{ct})$ mark the inner and outer classical turning points $R_{cti} = 3.2 \text{ \AA}$ and $R_{cto} = 9.1 \text{ \AA}$, respectively. The mean value of the internuclear distance is

$$\langle R(t) \rangle = \int dR |\chi(R, t)|^2 R \quad (3.7)$$

The mean values $\langle R(0) \rangle = R_{qti} = 3.3 \text{ \AA}$ at $t = 0$ and at the quantum-mechanical outer turning point, $\langle R(t_{qto}) \rangle = R_{qto} = 8.9 \text{ \AA}$ at $t_{qto} = 554$ fs, are close to the classical ones, R_{cti} and R_{cto} , respectively. The deviations are due to various effects, including wave packet tunneling from the classical turning point into the classically forbidden domain,²⁷ dispersion, and interferences.²⁸ The times when the mean value of the internuclear separation passes the values $\langle R(t_i) \rangle = R_i$, $\langle R(t_{\ddagger}) \rangle = R_{\ddagger}$, and $\langle R(t_o) \rangle = R_o$ for the first time are $t_i = 66$ fs, $t_{\ddagger} = 168$ fs, and $t_o = 334$ fs, respectively. The expected values R_i , R_{\ddagger} , and R_o and the corresponding times t_i , t_{\ddagger} , and t_o are indicated in Figures 1a,b, and 2a–e.

The time evolution of the NPD is illustrated in Figure 1a by a selection of snapshots at the times $t = 0$, t_i , t_{\ddagger} , t_o , and t_{qto} , when the nuclear wave packet is centered at the quantum-mechanical inner turning point R_{qti} , at the minimum of the inner potential well R_i , at the potential barrier R_{\ddagger} , at the minimum of the outer potential well R_o , and at the quantum-mechanical outer turning point R_{qto} , respectively. For convenience Figure 1a shows $\delta_n(R, t)$ times the factor $4\pi R^2$ (i.e., $|\chi(R, t)|^2 = 4\pi R^2 \delta_n(R, t)$; eq 2.14). The corresponding probability density of observing nucleus α ($=a, b$) at distance $R_\alpha = R/2$ from the NCM is shown in Figure 2b by color-coded contours of $4\pi R_\alpha^2 \delta_{n,\alpha}(R_\alpha, t)$ (eq 2.15). The mean value $\langle R_\alpha(t) \rangle = \langle R(t) \rangle/2$ is indicated by the continuous green line in Figure 2b. In accord with the Ehrenfest theorem, this line is close to the classical trajectory that starts out with zero velocity from R_{cti} at $t = 0$. It is apparent that, after an initial rather short period of acceleration, the nuclei separate at approximately constant speed until they decelerate at the outer turning point R_{qto} at $t_{qto} = 554$ fs. Scrutiny of $\langle R_\alpha(t) \rangle$ shows that the nuclei slow down slightly as they cross the barrier. After the turn at R_{qto} , the nuclei proceed toward the inner turning point R_{qti} . The quantum-mechanical time evolution of the “backward” motion from R_{qto} to

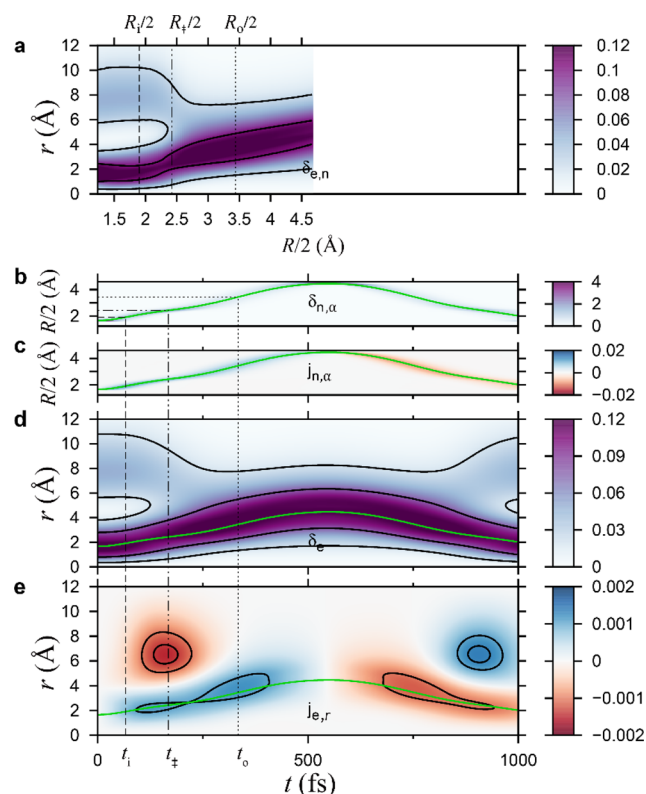


Figure 2. Color-coded contour plots of nuclear and electronic probability and flux densities for Na_2 in the electronic excited state $2^1\Sigma_u^+$ ($JM = 00$). (a) Static electronic population density $\delta_{e,n}(r;R/2)$ (eq 2.13) weighted by factor $4\pi r^2$ as a parametric function of the internuclear separation ($R/2$) (in units of $1/\text{\AA}$). Profiles along cuts at R_i , R_{\ddagger} , and R_o correspond to curves shown in Figure 1e. (b) Time evolution of nuclear probability density $\delta_{n,\alpha}(R_\alpha=R/2,t)$ weighted by factor $4\pi R_\alpha^2$ (in units of $1/\text{\AA}$). Its mean value is indicated by a continuous green line. (c) Time evolution of radial nuclear flux density $j_{n,\alpha}(R_\alpha=R/2,t)$, weighted by factor $4\pi R_\alpha^2$ (in units of $1/\text{fs}$). (d) Time evolution of electronic population density $\delta_e(r,t)$, weighted by factor $4\pi r^2$ (in units of $1/\text{\AA}$). (e) Time evolution of radial electronic flux density $j_{e,r}(r,t) \equiv j_e(r,t)$, weighted by factor $4\pi r^2$ (in units of $1/\text{fs}$).

R_{qti} is approximately the reverse of the “forward” motion from R_{qti} to R_{qto} . The corresponding classical trajectory is perfectly time reversible with respect to the time t_{cto} , when it coincides with the outer turning point, but in quantum mechanics the corresponding nuclear wave packets at the analogous times before and after t_{qto} differ from each other because of dispersion and interference effects.²⁸

The resulting radial flux density $j_{n,\alpha}(R_\alpha t)\mathbf{e}_R = 4j_n(2R_\alpha t)\mathbf{e}_R$ (eq 2.18) of the nuclei at distance $R_\alpha = R/2$ from the NCM is illustrated in Figure 2c by a color-coded contour map. For reference the mean value $\langle R_\alpha(t) \rangle$ is also shown as a continuous green line. The NFD follows the NPD, of course with a switch of sign (i.e., the NFD is positive as the bond stretches from R_{qti} to R_{qto} , and it is negative as the bond contracts from R_{qto} to R_{qti}). Although this observation appears to confirm intuition, it is nevertheless nontrivial in view of the subsequent counterexample (see below), where part of the electronic flux density (EFD) follows neither the NPD nor the EPD. Close inspection reveals local maxima in the absolute values of the NFD at the potential minima and local minima at the top of the potential barrier and the quantum-mechanical turning points. This observation may be rationalized by recalling that the corresponding classical flux

density is proportional to the classical probability density times the velocity. If we assume that the classical density is rather localized, as suggested by the quantum mechanical NPD shown in Figure 2b, then the time evolution of the classical flux density is dominated by the velocity, which has its local maxima at the potential minima and its local minima at the potential barrier and at the classical turning points.

We turn next to the computation of the EPD, which begins with the calculation of the one-electron probability density $d_{1e,n}(\mathbf{r};\mathbf{R})$ (eq 2.9) from the SAC-CI/aug-cc-pVTZ wave function $\Psi_e(\mathbf{r}^N;\mathbf{R})$. The EPD is divided into two parts³ corresponding to the 20 core electrons and the two valence electrons. It is known that the core electrons tend to travel with the nuclei.³ Here we center attention on the valence electrons ($N_e = 2$). Henceforth, the notation “ $d_{1e,n}(\mathbf{r};\mathbf{R})$ ” (and likewise the notation for quantities derived from $d_{1e,n}(\mathbf{r};\mathbf{R})$) refers to the one-electron probability density of the valence electrons.

For convenience we take \mathbf{R} to be aligned with the z -axis (i.e., $\mathbf{R} = R\mathbf{e}_z$). Then $d_{1e,n}(\mathbf{r};\mathbf{R})$ has cylindrical symmetry about the z -axis (internuclear axis). The one-electron probability density (multiplied by $N_e = 2$) is shown in Figure 1e as contour plots in the x - z plane for three characteristic internuclear distances: $R = R_i$, R_{\ddagger} , and R_o . At the shortest distance R_i (i.e., in the domain of the inner potential well) $d_{1e,n}(\mathbf{r};\mathbf{R})$ consists of three parts: a dominant inner one close to the NCM and two equivalent, much less intense, outer lobes well removed from the NCM. The inner part has two centers at the nuclei a and b. Away from the nuclei the closed, approximately ellipsoidal contours indicate molecular compactness. The outer lobes may be interpreted as signatures of the “Rydberg” character of the electronic structure in the domain of the inner potential well. Hence we shall call them “Rydberg lobes”. In contrast, at the largest distance R_o (i.e., in the domain of the outer potential well) the “Rydberg lobes” are absent, whereas the inner part of $d_{1e,n}(\mathbf{r};\mathbf{R})$ separates into two fragments that remain centered at the nuclei, thus indicating a highly stretched Na–Na bond. At the intermediate separation R_{\ddagger} (i.e., at the potential barrier between the inner and outer wells) the contour plot (Figure 1e) illustrates the transition from the character of $d_{1e,n}(\mathbf{r};\mathbf{R})$ at R_i to that at R_o . Apparently, the dominant inner centers of $d_{1e,n}(\mathbf{r};\mathbf{R})$ around the nuclei move outward as the bond stretches (i.e., they travel with the nuclei). At the same time the “Rydberg lobes” move inward until they are “absorbed” by the inner part and disappear approximately at the barrier.

It turns out that the properties of the one-electron probability density $d_{1e,n}(\mathbf{r};\mathbf{R})$ described just above are essential for the EPD and for the EFD. Before proceeding, we look in some depth at the origin of these characteristic properties. Because the SAC-CI/aug-cc-pVTZ implementation in the Gaussian suite²³ does not lend itself to the present purpose, we performed complementary state ($2^1\Sigma_u^+$) selective complete active space self-consistent-field (CASSCF-CI(2,36)) calculations, which permit a ready interpretation of the approximation $d_{1e,\text{CASSCF},n}(\mathbf{r};\mathbf{R})$ to $d_{1e,n}(\mathbf{r};\mathbf{R})$ obtained by the SAC-CI/aug-cc-pVTZ method. These CASSCF-CI(2,36) calculations for the Na_2 molecule aligned along the z -axis $\mathbf{R} = R\mathbf{e}_z$ are carried out by means of the MOLPRO suite²⁹ with the same aug-cc-pVTZ basis set and with inactive space consisting of the lowest ten molecular orbitals (MOs) $\phi_k(\mathbf{r};\mathbf{R})$ doubly occupied by all 20 core electrons and an active space of 36 MOs, labeled $k = 11$ (HOMO), 12 (LUMO), 13, ..., 46 for the two valence electrons. The final CASSCF wave function is expanded in terms of the pseudo-canonical MOs, as implemented by MOLPRO. Since the optimized CASSCF pseudo-canonical MOs $k = 11$ and $k = 12$

are similar to the corresponding HOMO and LUMO, for convenience we henceforward refer to them as such. It turns out that contributions of double excitations from the two valence electrons are negligible. The CASSCF-CI(2,36)/aug-cc-pVTZ electronic wave function can therefore be written approximately as a configuration-interaction (CI) expansion restricted to single excitations:

$$\Psi_{\text{e,CASSCF}}(\mathbf{r}^{22};R) \cong \sum_k D_{11}^k(R) [\Psi_{11,\alpha}^{k,\beta}(\mathbf{r}^{22};R) + \Psi_{11,\beta}^{k,\alpha}(\mathbf{r}^{22};R)] \quad (3.8)$$

Here $\Psi_{11,\alpha}^{k,\beta}(\mathbf{r}^{22};R)$ and $\Psi_{11,\beta}^{k,\alpha}(\mathbf{r}^{22};R)$ are the Slater determinants with all 20 core electrons occupying MOs $k = 1, \dots, 10$, and the two valence electrons occupying the molecular spin-orbitals $\varphi_{11}(\mathbf{r};R) \times \alpha$ and $\varphi_k(\mathbf{r};R) \times \beta$, or vice versa. The CI-expansion coefficients $D_{11}^k(R)$ are normalized according to

$$\sum_{k>11} P_{11}^k(R) = 1 \quad (3.9)$$

where

$$P_{11}^k(R) = 2[D_{11}^k(R)]^2 \quad (3.10)$$

is the CI-probability of the HOMO-to- k excitation. Integration of $[\Psi_{\text{e,CASSCF}}(\mathbf{r}^{22};R)]^2$ over the coordinates of all electrons but one (eq 2.9) yields, to a very good approximation, the CASSCF-CI/aug-cc-pVDT one-electron probability density of the valence electrons ($N_e = 2$),

$$d_{1\text{e,CASSCF},n}(\mathbf{r};R) \cong \frac{1}{N_e} \left[|\varphi_{11}(\mathbf{r};R)|^2 + \sum_k P_{11}^k(R) |\varphi_k(\mathbf{r};R)|^2 \right] \quad (3.11)$$

In principle, cross terms from MOs labeled 11 and k also contribute to the sum in eq 3.11, but they turn out to be negligible.

The beauty of this approximation (eq 3.11) is that it allows one to analyze the one-electron probability density in terms of the (squares of the) CI coefficients $D_{11}^k(R)$ and of the HOMO $\varphi_{11}(\mathbf{r};R)$ together with the excited MOs $\varphi_k(\mathbf{r};R)$, $k = 12, 13, 14, \dots$. This is illustrated in Figure 1b–d. Figure 1b shows the dominant populations of the HOMO ($k = 11$) and of the excited MOs ($=P_{11}^k(R)$, $k = 12$ and 14) together with the next highest populations (<0.02) of MOs $\varphi_k(\mathbf{r};R)$, $k = 18$ and 24. All other MOs are occupied with lower probability. Apparently, only three MOs ($k = 11, 12$, and 14) make the dominant contributions to $d_{1\text{e,CASSCF},n}(\mathbf{r};R)$. The corresponding orbital densities $d_{1\text{e,CASSCF},k}(\mathbf{r};R) = |\varphi_k(\mathbf{r};R)|^2$ are illustrated in Figure 1c for the characteristic internuclear distances $R = R_i$, R_{\ddagger} , and R_o . The weighted sum of these three orbital densities (i.e., eq 3.11) with the sum restricted to the two dominant contributions, $k = 12$ and 14, is shown in Figure 1d. Though the agreement with the SAC-CI/aug-cc-pVTZ one-electron probability density (Figure 1e) is not yet perfect, it is clear that $d_{1\text{e,CASSCF},n}(\mathbf{r};R)$ already exhibits the main features of $d_{1\text{e},n}(\mathbf{r};R)$. This suggests the following interpretation. The one-electron probability density $d_{1\text{e},n}(\mathbf{r};R)$ (multiplied by $N_e = 2$) of the valence electrons of $\text{Na}_2(2^1\Sigma_u^+)$ is essentially the weighted sum of three orbital densities, namely, of the HOMO ($k = 11$), the LUMO ($k = 12$), and the excited orbital $k = 14$. The three orbital probability densities maintain their dominant topologies as the internuclear distance increases from R_i to R_o . Thus, one may say that the probability density of the HOMO represents molecular compactness, except when the Na–Na bond is highly elongated at R_o . In contrast, the

probability density of the LUMO displays the topology of separated atoms, not only at $R = R_o$ but also already at $R = R_i$ and R_{\ddagger} . Finally, the probability density of the excited MO $k = 14$ represents typical features of a “Rydberg”-type MO, extending from the nuclei to intense lobes far from the nuclei. What really matters are the weightings of these MO densities. In the domain of the inner potential well, $d_{1\text{e},n}(\mathbf{r};R)$ is dominated by just two MO densities, namely, those of the HOMO and of the “Rydberg”-type MO ($k = 14$). This explains its characteristic features (i.e., the inner part and the two outer “Rydberg lobes”). In contrast, in the domain of the outer potential well, $d_{1\text{e},n}(\mathbf{r};R)$ is dominated by the orbital densities of the HOMO and the LUMO, whereas the “Rydberg”-type MO ($k = 14$) is negligible. This explains the topology of the contours of $d_{1\text{e},n}(\mathbf{r};R)$ at $R = R_o$, indicating the onset of separation of the Na atoms. Finally, at the transition $R = R_{\ddagger}$ from the domain near $R = R_i$ to that near R_o , the population of the “Rydberg”-type MO ($k = 14$) is depleted to the benefit of the HOMO. This explains the disappearance of the “Rydberg lobes” of $d_{1\text{e},n}(\mathbf{r};R)$ through a merging with the inner part of the one-electron probability density at the potential barrier.

The above interpretation is not quantitative, but it explains the most important features of the evolution of $d_{1\text{e},n}(\mathbf{r};R)$ as the internuclear separation increases from $R = R_i$ to $R = R_o$. We emphasize that subsequent calculations are based on $d_{1\text{e},n}(\mathbf{r};R)$ determined through the SAC-CI/aug-cc-pVDT method, rather than on the semiquantitative $d_{1\text{e,CASSCF},n}(\mathbf{r};R)$. We also remind the reader that $d_{1\text{e},n}(\mathbf{r};R)$ depends only on the distances r and R and the angle θ between the z -axis and the vector distance \mathbf{r} from the NCM to the electron. To emphasize the dependence of $d_{1\text{e},n}(\mathbf{r};R)$ on spherical coordinates, we henceforth denote it $\delta_{1\text{e},n}(r, \cos\theta; R)$ (eq 2.13).

According to eqs 2.11 and 2.13, we require the quantity $\delta_{\text{e},n}(r;R)$ to compute the EPD. We accomplish this task by fixing r and R and integrating $N_e \cdot \delta_{1\text{e},n}(r, \cos\theta; R)$ over the angle θ . The plots of $\delta_{\text{e},n}(r;R)$ versus r displayed in Figure 1e for the three characteristic internuclear distances $R = R_i$, R_{\ddagger} , and R_o depend strongly on R . At $R = R_i$ (the minimum of the inner potential well), $\delta_{\text{e},n}(r;R_i)$ is bimodal. The values of r at the two maxima and the minimum between them are indicated in Figure 1e by dotted lines, which also indicate the intersection of the x – z plane with the spherical surfaces on which $\delta_{\text{e},n}(r;R_i)$ is evaluated at these values of r . The inner maximum at the smallest r corresponds to the maximum of $\delta_{1\text{e},n}(r, \cos\theta; R_i)$ at the nuclei. The outer maximum at the largest r is due to the “Rydberg lobes” of $\delta_{1\text{e},n}(r, \cos\theta; R_i)$. In contrast, $\delta_{1\text{e},n}(r, \cos\theta; R_o)$ at the minimum R_o of the outer well does not possess “Rydberg lobes”. As a consequence, $\delta_{\text{e},n}(r;R_o)$ has just a single maximum, which corresponds to the maximum of $\delta_{1\text{e},n}(r, \cos\theta; R_o)$ at the nuclei. The transition from a bimodal to a unimodal $\delta_{\text{e},n}(r;R)$, which occurs close to the barrier at $R = R_{\ddagger}$ (Figure 1e), is illustrated in detail in Figure 2a, a color-coded contour plot of $\delta_{\text{e},n}(r;R_{\ddagger}=R/2)$. Apparently, $\delta_{\text{e},n}(r;R/2)$ has two branches, a dominant inner branch and a less prominent outer one at small and large r , respectively. The inner branch accounts for the valence electrons that travel with the nuclei from small to large values of R . The outer branch, due to the “Rydberg lobes”, is significant only in the domain of the inner potential well. Near the potential barrier it coalesces with the inner branch, which persists in the domain of the outer potential well.

The EPD $\delta_{\text{e}}(r,t)$ is given by eq 2.11 as an integral over R of the product of the *time-independent* electron population density $\delta_{\text{e},n}(r;R)$ and the *time-dependent* “nuclear probability density”

$(4\pi)^{-1}|\chi(R,t)|^2$. The EPD is exhibited in Figure 2d as a color-coded contour plot. One immediately observes the similarity of the topology of $\delta_e(r,t)$ in the temporal domain $0 < t < t_{\text{qto}}$ (Figure 2d) to that of $\delta_{e,n}(r;R_\alpha=R/2)$ in the corresponding spatial domain $R_{\text{qti}}/2 < R_\alpha < R_{\text{qto}}/2$ (Figure 2a). This correlation may be understood as follows. We note from Figure 2b that the NPD is extremely well localized. Hence we can make the approximation

$$|\chi(R,t)|^2 \simeq \delta[R - \langle R(t) \rangle] \quad (3.12)$$

where δ here denotes the Dirac distribution. Substitution of eq 3.12 into eq 2.11 yields

$$\delta_e(r,t) \simeq (4\pi)^{-1}\delta_{e,n}(r;\langle R(t) \rangle) \quad (3.13)$$

Thus, we see that the EPD at time t is proportional to $\delta_{e,n}(r;R)$ at the mean value of R at that time. As a consequence, all the properties of $\delta_{e,n}(r;R)$ also hold for $\delta_e(r,t)$. In particular, the EPD consists of two branches. The dominant branch accounts for the valence electrons that flow with the nuclei. This “normal” branch is centered at the mean distance of nucleus α from the NCM, which is indicated in Figure 2d by the continuous green line. The other branch is due to the “Rydberg lobe” in the domain of the inner potential well. This less intense “Rydberg” branch merges with the “normal” branch at the time t_\ddagger as the nuclei cross the potential barrier.

Equation 3.13 also holds for times $t > t_{\text{qto}}$, when $\langle R(t) \rangle$ decreases from the outer quantum mechanical turning point R_{qto} to the inner one R_{qti} . As shown in Figure 2d, the EPD in this temporal domain is approximately the mirror image of the EPD in the domain $t_{\text{qti}} < t < t_{\text{qto}}$. Deviations from perfect symmetry are due to nuclear wave packet dispersion and interference effects.²⁸

Finally, we use eq 2.16 to compute the EFD, which is displayed in Figure 2e as a color-coded contour plot. The EFD comprises two branches. One is due to the valence electrons that travel with the nuclei. (To guide the eye along this branch, Figure 2e shows the corresponding time evolution of the mean value $\langle R_\alpha(t) \rangle$ as a continuous green line). Accordingly, this “normal” branch is positive as R increases from R_{qti} to R_{qto} , negative as R decreases from R_{qto} to R_{qti} , and zero at the quantum-mechanical turning points. The second branch consists of a transient flux of electrons that rises and falls as the nuclei cross the barrier at R_\ddagger . Inspection of Figure 2d shows that this transient flow is due to the rapid change of the “Rydberg” branch of the EPD as it merges with the “normal” branch (i.e., the electronic structure changes from “Rydberg” to “ionic” as the nuclei traverse the potential barrier). The coalescence is actually supported by two effects. On one hand, as R increases in the domain $R_i < R < R_\ddagger$ the “normal” branch bends upward (toward increasing r). On the other hand, the “Rydberg” branch bends downward. As a consequence, the two components of the EFD (i.e., the “normal” component due to the valence electrons that travel with the nuclei, and the “transition” component that accounts for the change of the electronic structure at the barrier) are oppositely directed (i.e., they are antagonistic). We emphasize that this mechanism of production of antagonistic fluxes does not involve interference of the two components. An alternative mechanism, which is indeed due to interference of different partial waves, is documented in ref 3.

Figure 2e shows that the “transition” contribution to EFD is even stronger than the “normal” contribution. This seems surprising because Figure 2d suggests an opposite trend (i.e., the EPD in the “Rydberg” branch appears negligible compared with that of the “normal” branch). The apparent paradox can be

explained by the corresponding classical expression for the flux density, which is the product of the probability density, and the velocity. Hence, high (low) probability density does not necessarily imply high (low) flux density, respectively. Instead, high flux density may arise from low probability density that flows with high velocity. In the present case, the electrons in the low-density “Rydberg lobe” rearrange so rapidly during the transition from the “Rydberg” to the “ionic” structure that the absolute value of the “transition” component of the EFD is even larger than the “normal” component.

The principal results are summarized in Figure 3, which shows “arrow” plots of the NFD and EFD superposed on color-coded

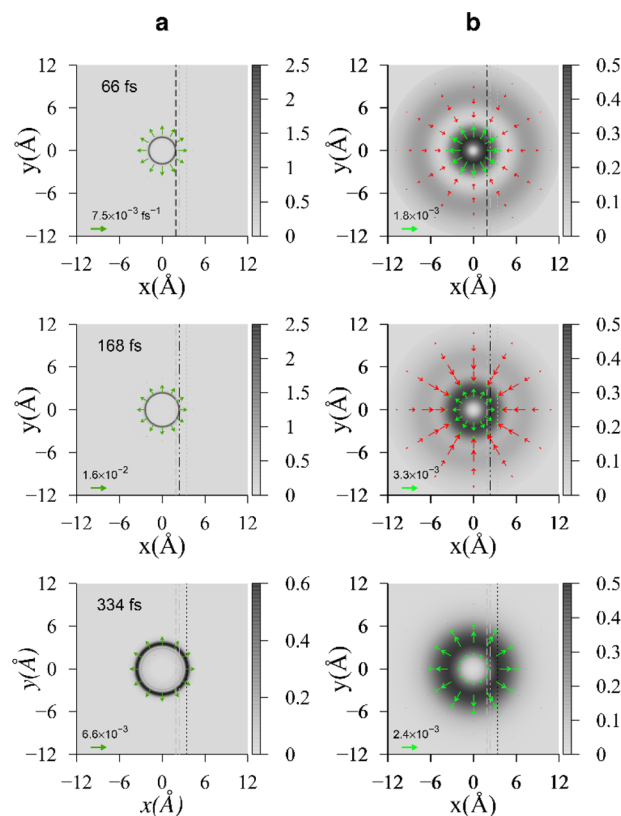


Figure 3. Color-coded contour plots combined with arrow plots of electronic population and nuclear probability densities and flux densities weighted by factor $4\pi r^2$ or $4\pi R_\alpha^2$ for Na_2 in the excited state $2^1\Sigma_u^+$ ($JM = 00$) at three characteristic times $t_i = 66$ fs, $t_\ddagger = 168$ fs, and $t_o = 334$ fs. (a) Nuclear probability density $[\delta_{n,\alpha}(R_\alpha=R/2,t)]$ and flux density $[j_{n,\alpha}(R_\alpha=R/2,t)]$ weighted by factor $4\pi R_\alpha^2$, in units of $1/\text{\AA}$ and $1/\text{fs}$, respectively. (b) Electronic population density (of valence electrons) $[\delta_e(r,t)]$ and electronic flux density $[j_e(r,t)]$ weighted by factor $4\pi r^2$, in units of $1/\text{\AA}$ and $1/\text{fs}$, respectively. Vertical lines indicate internuclear separations corresponding to the three characteristic times: $R_i/2$ (long dash); $R_\ddagger/2$ (dash-double dot); $R_o/2$ (short dash). Magnitudes of flux density are indicated by arrows at the bottom left of the plots.

contour plots of the NPD and EPD at the three characteristic times t_i , t_\ddagger , and t_o when the mean internuclear distance $\langle R(t) \rangle$ coincides with the minimum of the inner potential well at R_i , the top of the potential barrier at R_\ddagger and the minimum of the outer potential well at R_o , respectively. These snapshots demonstrate significant dispersion of the NPD; still, the NPD of the heavy nuclei are always far more localized than the EPD of the light electrons. The NFD is always unidirectional, with the nuclei flowing outward from R_{qti} toward R_{qto} . In contrast, the EFD at R_i

and at R_{\ddagger} are antagonistic, for the reasons that have been explained above in detail. The highest magnitudes of the EFD are caused by the transition of the electronic structure from “Rydberg” to “ionic” as the nuclei cross the potential barrier. At larger internuclear distances (e.g., at R_0) the EFD is unidirectional, like the NFD, because there are no further significant changes of the electronic structure. The valence electrons simply flow with the nuclei.

4. CONCLUSION

The present work extends the prior theory of concerted electronic and nuclear fluxes in the *one-electron*, nonrotating, diatomic $H_2^+ 2\Sigma_g^+$ ($JM = 00$) to the *multielectron*, nonrotating homonuclear diatomic in the state $2S+1\Sigma_{g,u}^+$ ($JM = 00$). The results for the many-electron system are entirely analogous to those for the one-electron system. In particular, the symmetry of the state implies that the EPD, NPD, and NFD are isotropic. A theorem due to Barth,⁴ based in part on ref 30, permits us to deduce that the EFD is also isotropic. The reduced radial continuity equation yields an expression for the EFD in terms of the EPD. Because all evolving quantities are isotropic, the system can be viewed as a pulsating or exploding “quantum bubble.”

As a first application of the theory we consider Na_2 vibrating in the double-minimum potential of the excited state $2^1\Sigma_u^+$. The most remarkable phenomenon is the two antagonistic contributions to the EFD. On the one hand, there is a component due to electrons that travel with the nuclei. This “normal” component is positive as the bond stretches and negative as it contracts. On the other hand, there is another, more intense, component appearing at greater distances from the NCM and opposing the “normal” component. We refer to this second contribution, which is transient (i.e., it rises and decays as the nuclei cross the barrier from one potential well to the other), as the “transition” component, because it is due to the change of electronic structure from “Rydberg” in the domain of the inner well to “ionic” in the domain of the outer well.

The present work should stimulate systematic investigations of concerted electronic and nuclear fluxes associated with adiabatic vibration and dissociation in other homonuclear diatomic molecules in their electronic ground and excited $2S+1\Sigma_{g,u}^+$ ($JM = 00$) states. The isotropy of the NPD and EPD suggests experimental measurements with high radial and temporal resolutions, where one needs to monitor the probability (or population) density only along one degree of freedom (see, for example, refs 31 and 32). The NFD and EFD can then be determined from the experimental NPD and EPD by means of the reduced radial continuity equation.³ The present application of the theory should also promote systematic searches for antagonistic electronic fluxes in more complicated systems and processes, such as adiabatic chemical reactions.

■ ASSOCIATED CONTENT

Supporting Information

The Supporting Information is available free of charge on the ACS Publications website at DOI: 10.1021/acs.jpca.7b11732.

Appendix A, demonstration of spherical symmetry of nuclear probability density, nuclear flux density, and electronic population density for a many-electron homonuclear diatomic molecule in a state $2S+1\Sigma_{g,u}^+$ ($JM = 00$); Appendix B, mean radial flux density from the continuity equation; Appendix C, preparation of the initial nuclear wave packet by a weak laser pulse (PDF)

■ AUTHOR INFORMATION

Corresponding Author

*J. Manz. E-mail address: jmanz@chemie.fu-berlin.de.

ORCID

D. J. Diestler: 0000-0002-3985-2812

J. Manz: 0000-0002-9142-8090

Notes

The authors declare no competing financial interest.

■ ACKNOWLEDGMENTS

The authors thank Dr. Ingo Barth (Halle), PD Dr. Dirk Andrae (Berlin) and Professor Beate Paulus (Berlin) for helpful discussions and Dr. Yasuki Arasaki (Tokyo), Professor Volker Engel (Würzburg), and Professor Matthias Wollenhaupt (Oldenburg) for valuable advice on the literature. Generous financial support from the Deutsche Forschungsgemeinschaft (project Ma 515/27-1), the National Key Research and Development of China (Grant No. 2017YFA0304203), the Program for Changjiang Scholars and Innovative Research Team (IRT13076), the National Natural Science Foundation of China (Grant Nos. 11434007, 61378039, 61575115) and the Shanxi 1331 Project is gratefully acknowledged.

■ REFERENCES

- (1) Manz, J.; Pérez-Torres, J. F.; Yang, Y. Vibrating $H_2^+ [2\Sigma_g^+(JM = 00)]$ Ion as a Pulsating Quantum Bubble in the Laboratory Frame. *J. Phys. Chem. A* **2014**, *118*, 8411–8425.
- (2) Pérez-Torres, J. F. Dissociating $H_2^+ [2\Sigma_g^+(JM = 00)]$ Ion as an Exploding Quantum Bubble. *J. Phys. Chem. A* **2015**, *119*, 2895–2901.
- (3) Bredtmann, T.; Diestler, D. J.; Li, S.-D.; Manz, J.; Pérez-Torres, J. F.; Tian, W.-J.; Wu, Y.-B.; Yang, Y.; Zhai, H. J. Quantum Theory of Concerted Electronic and Nuclear Fluxes Associated with Adiabatic Intramolecular Processes. *Phys. Chem. Chem. Phys.* **2015**, *17*, 29421–29464.
- (4) Barth, I. Probability and Flux Densities in the Center-of-Mass Frame. *J. Phys. Chem. A* **2018**, DOI: 10.1021/acs.jpca.7b11754.
- (5) Valance, A.; Nguyen Tuan, Q. The Molecular Electronic Structure of the Lowest $1,3\Sigma_{g,u}^+$ States of Na_2 and K_2 . *J. Phys. B: At. Mol. Phys.* **1982**, *15*, 17–33.
- (6) Jeung, G. Theoretical Study on Low-lying Electronic States of Na_2 . *J. Phys. B: At. Mol. Phys.* **1983**, *16*, 4289–4297.
- (7) Vergès, J.; Effantin, C.; Dİncan, J.; Cooper, D. L.; Barrow, R. F. Double-Minimum $1\Sigma_u^+$ State of Na_2 . *Phys. Rev. Lett.* **1984**, *53*, 46–47.
- (8) Cooper, D. L.; Barrow, R. F.; Vergès, J.; Effantin, C.; Dİncan, J. Laser-excited Fluorescence of the Double-Minimum $1\Sigma_u^+$ State of Na_2 Studied by Fourier Transform Spectroscopy. *Can. J. Phys.* **1984**, *62*, 1543–1562.
- (9) Assion, A.; Baumert, T.; Geisler, M.; Seyfried, V.; Gerber, G. Mapping of the Vibrational Wave-Packet Motion by Femtosecond Time-Resolved Kinetic Energy Time-of-Flight Mass Spectroscopy. *Eur. Phys. J. D* **1998**, *4*, 145–149.
- (10) Arasaki, Y.; Takatsuka, K.; Wang, K.; McKoy, V. Femtosecond Energy- and Angle-Resolved Photoelectron Spectra. *Chem. Phys. Lett.* **1999**, *302*, 363–374.
- (11) Takatsuka, K.; Arasaki, Y.; Wang, K.; McKoy, V. Probing Wavepacket Dynamics with Femtosecond Energy- and Angle-Resolved Photoelectron Spectroscopy. *Faraday Discuss.* **2000**, *115*, 1–15.
- (12) Arasaki, Y.; Takatsuka, K.; Wang, K.; McKoy, V. Femtosecond Energy- and Angle-Resolved Photoelectron Spectroscopy. *J. Chem. Phys.* **2000**, *112*, 8871–8883.
- (13) Arasaki, Y.; Takatsuka, K.; Wang, K.; McKoy, V. Probing Wavepacket Dynamics with Femtosecond Energy- and Angle-Resolved Photoelectron Spectroscopy. *J. Electron Spectrosc. Relat. Phenom.* **2000**, *108*, 89–98.

- (14) Arasaki, Y.; Takatsuka, K.; Wang, K.; McKoy, V. Energy- and Angle-Resolved Pump-Probe Photoelectron Spectroscopy: Molecular Rotation. *J. Chem. Phys.* **2001**, *114*, 7941–7950.
- (15) Wollenhaupt, M.; Assion, A.; Graefe, O.; Liese, D.; Sarpe-Tudoran, C.; Winter, M.; Baumert, T. Changes of the Electronic Structure along the Internuclear Coordinate Studied by Ultrafast Photoelectron Spectroscopy: the $^1\Sigma_u^+$ Double-Minimum State. *Chem. Phys. Lett.* **2003**, *376*, 457–464.
- (16) Wollenhaupt, M. *Observation and Coherent Control of Atomic and Molecular Dynamics*. Habilitation Thesis, Universität Kassel, Germany, 2004.
- (17) Wollenhaupt, M.; Engel, V.; Baumert, T. Femtosecond Laser Photoelectron Spectroscopy on Atoms and Small Molecules: Prototype Studies in Quantum Control. *Annu. Rev. Phys. Chem.* **2005**, *56*, 25–56.
- (18) Jia, D.; Manz, J.; Yang, Y. Communication: Electronic Flux Induced by Crossing the Transition State. *J. Chem. Phys.* **2018**, *148*, 041101.
- (19) Okuyama, M.; Takatsuka, K. Electron Flux in Molecules Induced by Nuclear Motions. *Chem. Phys. Lett.* **2009**, *476*, 109–115.
- (20) Takatsuka, K.; Yonehara, T. Exploring Dynamical Electron Theory Beyond the Born-Oppenheimer Framework: From Chemical Reactivity to Non-adiabatically Coupled Electronic and Nuclear Wavepackets On-the-fly Under Laser Field. *Phys. Chem. Chem. Phys.* **2011**, *13*, 4987–5016.
- (21) Nagashima, K.; Takatsuka, K. Early-Stage Dynamics in Coupled Proton-Electron Transfer From π - π^* State of Phenol to Solvent Ammonia Clusters: A Nonadiabatic Electron Dynamics Study. *J. Phys. Chem. A* **2012**, *116*, 11167–11179.
- (22) Takatsuka, K.; Yonehara, T.; Hanasaki, K.; Arasaki, Y. *Chemical Theory Beyond the Born-Oppenheimer Paradigm: Nonadiabatic Electronic and Nuclear Dynamics in Chemical Reactions*; World Scientific: Singapore, 2015.
- (23) Frisch, M. J.; Trucks, G. W.; Schlegel, H. B.; Scuseria, G. E.; Robb, M. A.; Cheeseman, J. R.; Scalmani, G.; Barone, V.; Mennucci, B.; Petersson, G. A.; et al. *Gaussian 09*, Revision D.01; Gaussian Inc.; Wallingford, CT, 2010.
- (24) Nakatsuji, H. Cluster Expansion of the Wavefunction. Electron Correlations in Ground and Excited States by SAC (symmetry-adapted-cluster) and SAC CI. *Chem. Phys. Lett.* **1979**, *67*, 329–333.
- (25) Kendall, R. A.; Dunning, T. H., Jr; Harrison, R. J. Electron Affinities of the First-row Atoms Revisited. Systematic Basis Sets and Wave Functions. *J. Chem. Phys.* **1992**, *96*, 6796–6806.
- (26) Marston, C. C.; Balint-Kurti, G. G. The Fourier Grid Hamiltonian Method for Bound State Eigenvalues and Eigenfunctions. *J. Chem. Phys.* **1989**, *91*, 3571–3576.
- (27) Child, M. S. *Molecular Collision Theory*; Academic Press: London, 1974.
- (28) Manz, J.; Pérez-Torres, J. F.; Yang, Y. Nuclear Fluxes in Diatomic Molecules Deduced from Pump-Probe Spectra with Spatiotemporal Resolutions down to 5 pm and 200 as. *Phys. Rev. Lett.* **2013**, *111*, 153004.
- (29) Werner, H. J.; Knowles, P. J.; Knizia, G.; Manby, F. R.; Schütz, M.; Celani, P.; Korona, T.; Lindh, R.; Mitrushenkov, A.; Rauhut, G.; et al. *MOLPRO, version 2012.1, A package of ab initio programs*, <http://www.molpro.net>, 2012.
- (30) Barth, I.; Renziehausen, K. On the Exact Rotational and Internal Hamiltonian for a Non-Relativistic Closed Many-Body System. *J. Phys.: Conf. Ser.* **2017**, *869*, 012006.
- (31) Frohnmeyer, T.; Baumert, T. Femtosecond Pump-Probe Photoelectron Spectroscopy on Na_2 : A Tool to Study Basic Coherent Control Schemes. *Appl. Phys. B: Lasers Opt.* **2000**, *71*, 259–266.
- (32) Ergler, T.; Rudenko, A.; Feuerstein, B.; Zrost, K.; Schröter, C. D.; Moshhammer, R.; Ullrich, J. Spatiotemporal Imaging of Ultrafast Molecular Motion: Collapse and Revival of the D_2^+ Nuclear Wave Packet. *Phys. Rev. Lett.* **2006**, *97*, 193001.